Competing failure mechanisms in mixed-mode fracture of an adhesively-bonded polymer-matrix composite

S. Li[1], M. D. Thouless[1,2], A. M. Waas[3], J. A. Schroeder[4], and P. D. Zavattieri[4]

[1]*Department of Mechanical Engineering*
[2]*Department of Materials Science & Engineering*
[3]*Department of Aerospace Engineering*
University of Michigan, Ann Arbor, MI 48109

[4]*General Motors Research and Development*
Warren, MI 48090

Abstract

In this paper, the use of cohesive-zone models to analyze crack-path selection in adhesive joints made from a polymer-matrix composite is demonstrated. Cohesive-zone parameters for the adhesive and composite obtained in previous work were used without any modifications to make the predictions presented in this study. The results of numerical simulations of two mixed-mode geometries, single-lap shear and asymmetrical double-cantilever beam specimens, are compared to experimental observations. It is shown that the numerical simulations provided reasonably good predictions for the strength and failure mechanisms of the joints, allowing the nature of the competition between failure of the composite and failure of the interface to be determined.

(July 2005)

1. Introduction

The problem of crack-path selection has long been of great interest in the interfacial mechanics community. In many cases, the crack propagates along the interface between two adherends. However, in other cases, the crack may deflect out of the interface and into the adjoining material. A number of studies of how a crack may kink off an interface have been done using linear-elastic fracture mechanics (LEFM) in which fracture is characterized by a single material property - the toughness, Γ. The competition between crack propagation along the interface and deflection into the adherend depends on the relative toughness of the interface to that of the surrounding adherend [1-3]. Specifically, deflection off the interface along a mode-I path will occur if

$$\mathcal{G}_i \,/\, \mathcal{G}_t < \Gamma_i \,/\, \Gamma_a \,, \tag{1}$$

where $\mathcal{G}_i$ is energy release rate at the interface crack tip, $\mathcal{G}_t$ is the energy release rate at the kinked crack tip, Γ_i is the toughness of the interface at the appropriate level of mode mix, and Γ_a is the mode-I toughness of the adherend [1]. This approach implicitly assumes the existence of initial kinks in the adherends that are long enough for valid expressions for the energy-release rate to be calculated. However, it should be noted that real materials have cohesive strengths, $\hat{\sigma}$, that affect crack propagation if a characteristic fracture-length scale, defined as $E\Gamma/\hat{\sigma}^2$ (where E is the appropriate modulus of the adherends), is much smaller than the characteristic length of the geometry. In particular, energy-based deflection criteria are only appropriate if the fracture-length scale is much smaller than the kink length. In a reasonably tough material, suitably long kinks may not exist,

and an alternative criterion for determining the onset of crack kinking out of an interface is required.

Based on the original insights of Dugdale [4] and Barenblatt [5], cohesive-zone models provide an ideal tool to study crack deflection problems in weak, tough materials, as they implicitly incorporate the appropriate strength and toughness criteria. In the work of Parmigiani and Thouless [6], it was shown that crack deflection *into* an interface is generally dominated by cohesive strength considerations, rather than by toughness considerations. Furthermore, cohesive-zone models have also been demonstrated to have the capability to predict arbitrary crack trajectories. For example, in the studies of Xu and Needleman [7], interfacial cohesive elements were embedded between pairs of neighboring continuum elements in the mesh. The crack then extended along the element boundaries without remeshing. A similar technique has been used to predict the dynamic failure of brittle materials [8, 9].

In the present work, it is shown that cohesive-zone models can be used to predict whether an interfacial crack will continue propagating along the interface, or whether it will kink into the adherends. This allows the effects of competing failure mechanisms in an adhesively-bonded composite to be considered under mixed-mode loading. In previous work by the authors, cohesive-zone models for an adhesive interface [10, 11] and composite [12] were developed. Here, these models are used without modification to analyze crack-path selection under mixed-mode conditions, with specific studies on different mixed-mode bonded geometries.

2. Fracture parameters and the mixed-mode cohesive-zone model

The composite used for the adherends in this study was a polypropylene matrix with randomly-oriented glass fibers.[1] Details of the constitutive and fracture properties of this composite have been described in previous work [12]. The composite can be characterized as being transversely isotropic and linear-elastic in plane, with an in-plane tensile modulus of 6.0 ± 1.5 GPa, an in-plane Poisson's ratio of 0.30 ± 0.03, and an in-plane shear yield strength of 65 ± 15 MPa. The out-of-plane tensile modulus is 4 ± 1GPa, while the out-of-plane shear modulus is 0.5 ± 0.1GPa [13]. As discussed in Section 3.2, only mode-I fracture of the composite, appropriate for the initial stages of composite failure, is addressed in this paper. The mode-I fracture of the composite can be described by a cohesive law of the form shown in Fig. 1, which captures the observed behavior of matrix cracking followed by fiber pull-out. The three important parameters that describe the mode-I cohesive law for the composite are the matrix-cracking strength, $\hat{\sigma}_m$ =100 ± 20 MPa, the fiber-bridging strength, $\hat{\sigma}_b = 79 \pm 8$ MPa, and the toughness, $\Gamma_{Ic} = 40 \pm 4$ kJm^{-2}.

The adhesive used in this study was an experimental, two-part adhesive.[2] This adhesive cures at room temperature, and was specially formulated to bond low-surface-energy materials such as polypropylene. In all studies, the thickness of the adhesive layer was maintained at 0.6 to 0.8 mm by using uniform-sized glass beads as spacers. The mode-I and mode-II traction-separation laws of the adhesively-bonded interface are shown in Fig. 2. These laws represent the deformation of the entire adhesive layer (the cohesive elements replace the entire

[1] Azdel R401 provided by Azdel, Inc.
[2] Provided by Dow Chemical Company.

adhesive layer in the numerical model) under the appropriate constraint acting on the layer; they were deduced for the particular thickness of adhesive layer used in these studies. The mode-I law, which represents interfacial cracking followed by fiber pull-out [10], is described by three important parameters: the intrinsic cohesive strength of the interface, $\hat{\sigma}_{io}$ =24 ± 3 MPa, the characteristic interface strength, $\hat{\sigma}_i$ = 5.0 ± 1.5 MPa, and the toughness, Γ_{Ii} = 7.3 ± 1.8 kJm^{-2}. The mode-II interfacial tests indicated that few fibers are pulled out during mode-II fracture; therefore, a simpler trapezoidal traction-separation law was chosen to simulate the elastic/plastic behavior of the mode-II debonding process [11]. The two important parameters that describe this cohesive law are the characteristic interface strength, $\hat{\tau}_i$= 12 ± 1.5 MPa, and the toughness, Γ_{IIi}= 11.5 ± 1.5 kJm^{-2}.

The mixed-mode cohesive-zone model has been described elsewhere [14, 15]. Specifically, it is incorporated through a 4-node, user-defined element in ABAQUS. The normal tractions, σ, depend only on the relative opening displacements, δ_n; the shear tractions, τ, depend only on the relative shear displacements, δ_τ. The opening and shear traction-separation laws are independent of each other, except they are coupled through a simple failure criterion of the form

$$\mathcal{G}_I/\Gamma_I + \mathcal{G}_{II}/\Gamma_{II} = 1 \quad . \tag{2}$$

In this failure criterion, Γ_I and Γ_{II} (the mode-I and mode-II toughness) represent the total areas under the traction-separation curve for each mode (Fig. 2), and the mode-I and mode-II energy-release rates are given by

$$\mathcal{G}_I = \int_0^{\delta_n} \sigma(\delta'_n)\, d\delta'_n; \qquad \mathcal{G}_{II} = \int_0^{\delta_t} \tau(\delta'_t)\, d\delta'_t \quad . \tag{3}$$

Once the failure condition of Eqn. (2) is met, the element is considered to be no longer capable of bearing a load, and the crack advances. In the analyses that follow, all the cohesive laws described above have been used without any modification. Absolutely no fitting to any experimental results has been done in this paper. Experimental observations have been compared to numerical predictions based only on parameters obtained in earlier studies.

3. Numerical studies of mixed-mode fracture

3.1 Numerical predictions with only interface cohesive-zone elements

The first phase of the numerical simulations was done ignoring the possibility of composite failure. These initial calculations provided information about the stress state in the composite arms, and about the nature of any interfacial fracture that might occur. Only continuum elements with the constitutive properties of the composite [12] were used to model the adherends, with no failure criterion being invoked. The adhesive layer was modeled using interfacial cohesive elements with the appropriate mode-I and mode-II parameters [10, 11] in conjunction with the failure criterion of Eqn. (2). ABAQUS 6.4 was chosen to perform the analysis allowing large-scale, non-linear deformations to occur, and the effects of uncertainty and variation in the cohesive parameters were all explored. It was also verified that any effects of mesh size were negligible compared with other sources of uncertainty.

The dimensions of the specimens for these numerical computations are shown in Fig. 3. For the single-lap shear specimens, the width of the specimens was 25 ± 0.5 mm, the overlap length was 25 ± 1 mm and the free portion of the arms was 70 ± 1 mm (Fig. 3a). Two different thicknesses of arms, 2.8 ± 0.2 mm

and 5.0 ± 0.2 mm, were used. The dimensions of the asymmetrical double-cantilever beam (ADCB) specimens were as follows: the thickness of the thinner arm, h_1, was 5.0 ± 0.3 mm, the thickness of the thicker arm, h_2, was 7.6 ± 0.3 mm, the width, W, was 25.2 ± 0.5 mm, the initial crack length, a_0, was 40 ± 3 mm, and the bonded length, b_0, was 120 ± 2 mm (Fig. 3b).

Figure 4 shows predictions of the load-displacement curves for the three different geometries if composite failure is suppressed.[3] The effects of the possible range of interface parameters on the behavior are indicated by the upper and lower bounds of these curves. The plateaus in the numerical curves for both the single-lap shear specimens are caused by the development of the cohesive-zone. No stable crack growth was predicted by these calculations for either of the single-lap shear geometries, within the range of possible interfacial cohesive properties. This was indicated by the fact that the numerical predictions terminated abruptly once the crack started to propagate. A careful numerical evolution of this instability using Riks method showed that this instability had a physical basis, and was therefore associated with a predicted transition to dynamic fracture. As discussed in Li *et al*. [12], this type of transition occurs when the elastic energy stored by the specimen (and loading device) exceeds the energy required to fracture the remaining ligament of the interface. This results in catastrophic failure with no further work being done by the applied loads. Any excess energy is dissipated kinetically when the crack propagates under non-equilibrium conditions. These results, therefore, indicate that if interfacial

[3] The different gauge lengths for the two single-lap shear specimens were chosen to be consistent with the methods that would be used to evaluate the displacements on the experimental specimens.

fracture occurs in the single-lap shear geometries, it does so in a catastrophic fashion. In contrast to this type of behavior, stable crack growth along the entire interface was predicted for the asymmetrical double-cantilever beam. No tendency for a transition to unstable behavior was predicted by the numerical calculations.

3.2 Numerical predictions with both interface and composite cohesive-zone elements

In the calculations described in the previous section, it was observed that the maximum normal stresses in the composite were aligned approximately parallel to the interface, near the crack tip in the asymmetrical double-cantilever beam and at the bonded corner of the lap-shear specimen. Therefore, additional user-defined elements, describing the mode-I cohesive properties of the composite (Fig. 1), were embedded in the composite at these locations for each geometry, and were aligned perpendicular to the interface. This use of mode-I elements aligned in this fashion was not expected to capture the full details of the composite failure (which involved some mode-II delamination); however, it was expected to describe crack initiation, so that transitions in failure mechanisms could be analyzed. To keep the numerical model to a reasonable size, the region in which the cohesive-zone elements were embedded was limited to 10 mm in length. Once the calculations had begun, the propagation of the crack was monitored, and the program was terminated if the interfacial crack tip passed the region in which cohesive-zone elements were embedded in the composite. The model was then re-meshed with a new region of composite cohesive-zone elements, and the analysis re-started. This process was repeated until the crack

had either grown completely along the interface, had caused catastrophic failure of the interface (as discussed above), or had caused fracture of the composite.

The predictions for the load-displacement plots of the three geometries are given in Fig. 5. These plots show the range of behavior expected for the variations in the interfacial and composite fracture properties. The calculations indicate that the strength of the 2.8 mm single-lap shear specimens is dictated by the composite. For all combinations of the cohesive properties of the interface and the composite, the arms always fracture before any crack propagation occurs along the interface. The failure mechanisms predicted by the numerical simulations for the 5 mm single-lap shear geometry depend on the relative strengths of the composite and interface, with a general tendency for composite fracture. For a relatively "weak" interface and a "strong" composite failure occurs by catastrophic interfacial fracture. However, for other combinations of composite and interface properties, the numerical results predict failure of the composite. The results of the numerical simulations for the asymmetrical double-cantilever beam specimens also depend on the relative strengths of the composite and interface. Again, there is a tendency for composite fracture to occur. For a "strong" composite and a "weak" interface the numerical results indicate that an interfacial crack will propagate stably without deviating into the composite. At the other extreme, for a "weak" composite and a "strong" interface, the composite is predicted to fail without any interfacial crack growth. An intermediate behavior is predicted for intermediate properties of the composite and interface, with the crack deviating into the composite after a limited amount of propagation along the interface. It should be noted that this

transition to composite fracture is predicted to occur even for a specimen with uniform properties along the interface.

In conclusion, the numerical calculations indicate that the 2.8 mm thick single-lap shear specimens with the geometry given in Fig. 3(a) will always fail in the composite with no interfacial delamination occurring. The 5.0 mm thick single-lap shear specimens with the geometry given in Fig. 3(a) can exhibit either composite failure or interfacial failure, depending on the precise values of the fracture parameters within the measured range. However, the calculations clearly indicate that if interfacial fracture occurs, it will do so in a catastrophic (dynamic) fashion, with no tendency for quasi-static, stable crack propagation. At the extreme ranges of the possible cohesive parameters, the asymmetrical double-cantilever beam specimens with the geometry given in Fig.3(b) are predicted to exhibit either composite failure or stable interfacial failure. However, for intermediate values of the cohesive properties, these specimens are expected to fail by the crack propagating stably down the interface for a finite distance and then deviating into the composite arms. No catastrophic (dynamic) fracture of the interface in this geometry is predicted to occur under quasi-static loading conditions.

4. Experimental results

Two sets of single-lap shear specimens of the geometry described in Fig. 3a were fabricated. One set of specimens was made from composite plaques that were 2.8 mm thick; another set were made from composite plaques that were 5.0 mm thick. In addition, a set of asymmetrical double-cantilever beams specimens with the geometry described in Fig. 3b were also fabricated. Teflon

tape was used to prevent the adhesive from extruding onto the free arms. All specimens were tested on a screw-driven MTS machine in displacement control at a constant cross-head velocity of 1.0 mm/minute at room temperature until failure occurred. The displacement for the 2.8 mm single-lap shear specimens was measured optically between two points separated by a gauge length of 75 mm, while the displacement for the 5 mm single-lap shear specimens was measured with an extensometer having a gauge length of 25 mm. The loading-line displacement of the asymmetrical double-cantilever beam specimens was measured from the cross-head of the testing machine, as calibrated by optical measurements. A high resolution C.C.D camera was used for the optical measurements, and to monitor the crack initiation and crack propagation.

When the 2.8 mm thick single-lap shear specimens were tested, catastrophic failure of the composite occurred near the bond (Fig. 6a). No interfacial crack propagation was observed in these specimens. When the 5 mm thick single-lap shear specimens were tested, catastrophic interfacial failure occurred as soon as the interfacial crack started to propagate (Fig. 6b). All the asymmetrical double-cantilever beam specimens failed in the composite after some interface crack propagation. In these specimens, the crack initially propagated in a stable fashion along the interface for about 15 ~ 30 mm (Fig. 7a). The crack was then arrested, and damage began to accumulate in the thinner arm at the crack tip until the composite failed (Fig. 7b). These experimental observations are all consistent with the numerical predictions described in the previous section. The only possible minor discrepancy between the predictions and the observations is that the numerical predictions suggested a possible

tendency for composite fracture in the 5.0 mm single-lap shear specimens. This was not observed experimentally in the three specimens tested, only catastrophic interfacial failure (that was also predicted by the numerical calculations as a possible failure mechanism) was observed. While it is possible that this was a statistical effect associated with the properties of the composite and interface, there may also be an effect of the severe stress concentrations in the numerical model associated with the sharp corners of the geometry. If this were so, the numerical results might be improved by the use of rounded corners. However, such attempts at fine-tuning the numerical models after experimental observations were not the focus of this work. Overall, the numerical analysis appears to have captured the underlying physics of the different failure mechanisms, giving reasonable predictions for the experimental results.

The other point of comparison between the numerical predictions and the experimental results is provided by the load *versus* displacement curves. Figures 8(a) and 8(b) show the load-per-unit-width *versus* displacement curves for the 2.8 mm and the 5 mm single-lap shear specimens. Figure 8(c) shows the load-per-unit-width *versus* loading-line-displacement data from the asymmetrical double-cantilever beam joints. Superimposed on these plots are the numerical predictions from the previous section. As discussed earlier, the numerical calculations were not designed to capture the failure of the composite after crack initiation; to fit this portion of the curves in Fig. 8(c) would require additional details about mixed-mode fracture and delamination in the composite. Furthermore, a comparison between the details of the plateaus in the load-displacement curves shown in Fig. 8(b), where the cohesive zone is developing

before catastrophic fracture of the interface, provides an example of where the details of the cohesive law may play a role. The numerical calculation involved a trapezoidal mode-II cohesive law; the shape of the experimental curve when the cohesive zone is developing suggests that a slightly different shape might be appropriate. However, despite these minor issues, Fig. 8 clearly demonstrates that the numerical results not only predicted the failure mechanisms reasonably well, but also provided good predictions for the loads and deformation involved in the failure of joints.

5. Conclusions

In this paper, mixed-mode cohesive-zone models were used to examine the competing failure mechanisms of interfacial fracture and fracture of the composite arms. Interfacial cohesive parameters and the mode-I cohesive-zone properties for the composite, obtained from previous work, were used without any modifications in the numerical studies. The numerical results predicted the behavior of two mixed-mode geometries: single-lap shear joints and asymmetrical double-cantilever beam joints. Not only were the strengths and deformations reasonably well described, but the nature of the competition between failure of the composite and failure of the interface could also be captured. In particular, the asymmetrical double-cantilever beam geometry showed a strong tendency for composite failure, even with relatively thick arms. An interfacial crack deviated into the composite arms, even though the ratio of the toughness of the composite to interface was about 5:1. At this ratio of toughnesses, an energy-based failure criterion would not predict failure of the adherends at the level of mode-mixedness appropriate for these geometries. The

introduction of a characteristic strength associated with cohesive-zone models may provide an approach for predicting the mixed-mode strength of adhesively-bonded composite joints, allowing competing failure mechanisms to be addressed.

Acknowledgements

S. L., M. D. T. and A. M. W. gratefully acknowledge the financial support of General Motors, the supply of the composite from Azdel, Inc., and the supply of the adhesive from Dow Chemical. In addition, we would like to thank R.P. Atkins for help with sample preparation and H. Elias for help with molding, respectively.

References

1. He, M.-Y., and J. W. Hutchinson, "Kinking of a crack out of an interface," *Journal of Applied Mechanics*, **56**, 270-278 (1989).

2. Thouless, M. D., H. C. Cao and P. A. Mataga, "Delamination from surface cracks in composite materials," *Journal of Materials Science*, **24**, 1406-1412 (1989).

3. Xie, D., Waas, A. M., Shahwan, K. W., Schroeder, J. A. and Boeman, R. G. "Fracture criterion for kinking cracks in a tri-material adhesively bonded joint under mixed mode loading," *Journal of Engineering Fracture Mechanics* (in press).

4. Dugdale, D. S., "Yielding of steel sheets containing slits," *Journal of the Mechanics and Physics of Solids*, **8**, 100-108 (1960).

5. Barenblatt, G. I., "The mathematical theory of equilibrium of cracks in brittle fracture," *Advances in Applied Mechanics*, **7**, 55-129 (1962).

6. Parmigiani, J. and M. D. Thouless, "The roles of toughness and cohesive strength on crack deflection at interfaces," manuscript under review.

7. Xu, X. P. and A. Needleman, "Numerical simulations of fast crack growth in brittle solids," *Journal of Mechanics and Physics of Solids*, **42**, 1397-1434 (1994).

8. Camacho, G. T. and M. Ortiz, "Computational modeling of impact damage in brittle materials," *International Journal of Solids and Structures*, **33**, 2899-2938 (1996).

9. Zavattieri, P. D. and H. D. Espinosa, "Grain lever analysis of crack initiation and propagation in brittle materials," *Acta Materialia*, **49**, 4291-4311 (2001).

10. Li, S., M. D. Thouless, A. M. Waas, J. A. Schroeder, and P. D. Zavattieri, "Use of mode-I cohesive-zone models to describe the fracture of an adhesively-bonded polymer-matrix composite," *Composite Science and Technology*, **65**, 281-293, (2005).

11. Li, S., M. D. Thouless, A. M. Waas, J. A. Schroeder, and P. D. Zavattieri, "Mixed-mode cohesive-zone models for fracture of an adhesively-bonded

polymer-matrix composite," *Journal of Engineering Fracture Mechanics* (in press).

12. Li, S., M. D. Thouless, A. M. Waas, J. A. Schroeder, and P. D. Zavattieri, "Use of a cohesive-zone model to analyze the fracture of a fiber-reinforced polymer-matrix composite," *Composite Science and Technology*, **65**, 537-549 (2005).

13. Sun, C., unpublished work (2004).

14. Yang, Q. D. and M. D. Thouless, "Mixed-mode fracture analyses of plastically-deforming adhesive joints," *International Journal of Fracture*, **110**, 175-187 (2001).

15. Li, S., "Fracture analysis of an adhesively-bonded polymer-matrix composite," Ph.D. dissertation, University of Michigan, Ann Arbor, MI (2004).

Figure captions

Figure 1 Traction-separation law used to describe the mode-I fracture of this composite (from Li *et al.*, 2005b).

Figure 2 Traction-separation laws used to describe the mode-I (from Li *et al.*, 2005a) and mode-II (from Li *et al.*, 2005c) fracture of the adhesive interface studied in this paper.

Figure 3 Geometry and dimensions for **(a)** the single-lap shear specimens, and **(b)** the asymmetrical double-cantilever beam specimens used to investigate the mixed-mode fracture properties of the adhesive-composite interface.

Figure 4 Load (per unit width) *versus* displacement for **(a)** 2.8 mm thick single-lap shear specimens for a gauge length of 75 mm with the geometry shown in Fig. 3(a), **(b)** 5 mm thick single-lap shear specimens for a gauge length of 25 mm with the geometry shown in Fig. 3(a), and **(c)** asymmetrical double-cantilever beam specimens with the geometry shown in Fig. 3(b). The solid lines indicate the numerical predictions without embedding cohesive-zone elements into the composite. The two limits show the uncertainties of cohesive zone properties of the interface.

Figure 5 Numerical predictions for the load (per unit width) *versus* displacement incorporating cohesive zones for both the composite and the interface. The effect of the extent of the cohesive parameters is demonstrated by the extreme limits of the different

curves. The predicted failure mechanisms are indicated on each plot. **(a)** 2.8 mm thick single-lap shear specimens; **(b)** 5 mm thick single-lap shear specimens; **(c)** asymmetrical double-cantilever beam specimens. The solid lines indicate the numerical predictions without embedding cohesive-zone elements into the composite. The two limits show the uncertainties of cohesive-zone properties of the interface.

Figure 6 Micrographs of a damaged single-lap shear specimen with **(a)** 2.8 mm thick arms, showing composite fracture near the bonded joint, and **(b)** 5 mm thick arm, showing interfacial fracture. (Scales are in cm.)

Figure 7 Micrographs of an asymmetrical double-cantilever beam specimen during **(a)** an intermediate stage of crack propagation, and **(b)** the final stage of failure, showing fracture of the composite at the crack tip near the bottom of the thinner arm. (Scales are in cm.)

Figure 8 Comparisons between the numerical results and the numerical predictions for the load (per unit width) *versus* displacement for **(a)** 2.8 mm thick single-lap shear specimens for a gauge length of 75 mm, **(b)** 5 mm single-lap shear specimens for a gauge length of 25 mm, and **(c)** asymmetrical double-cantilever beam specimens with the geometry shown in Fig. 3(b). The dotted lines or data points show the experimental results. The solid lines indicate the numerical predictions of Fig. 5.

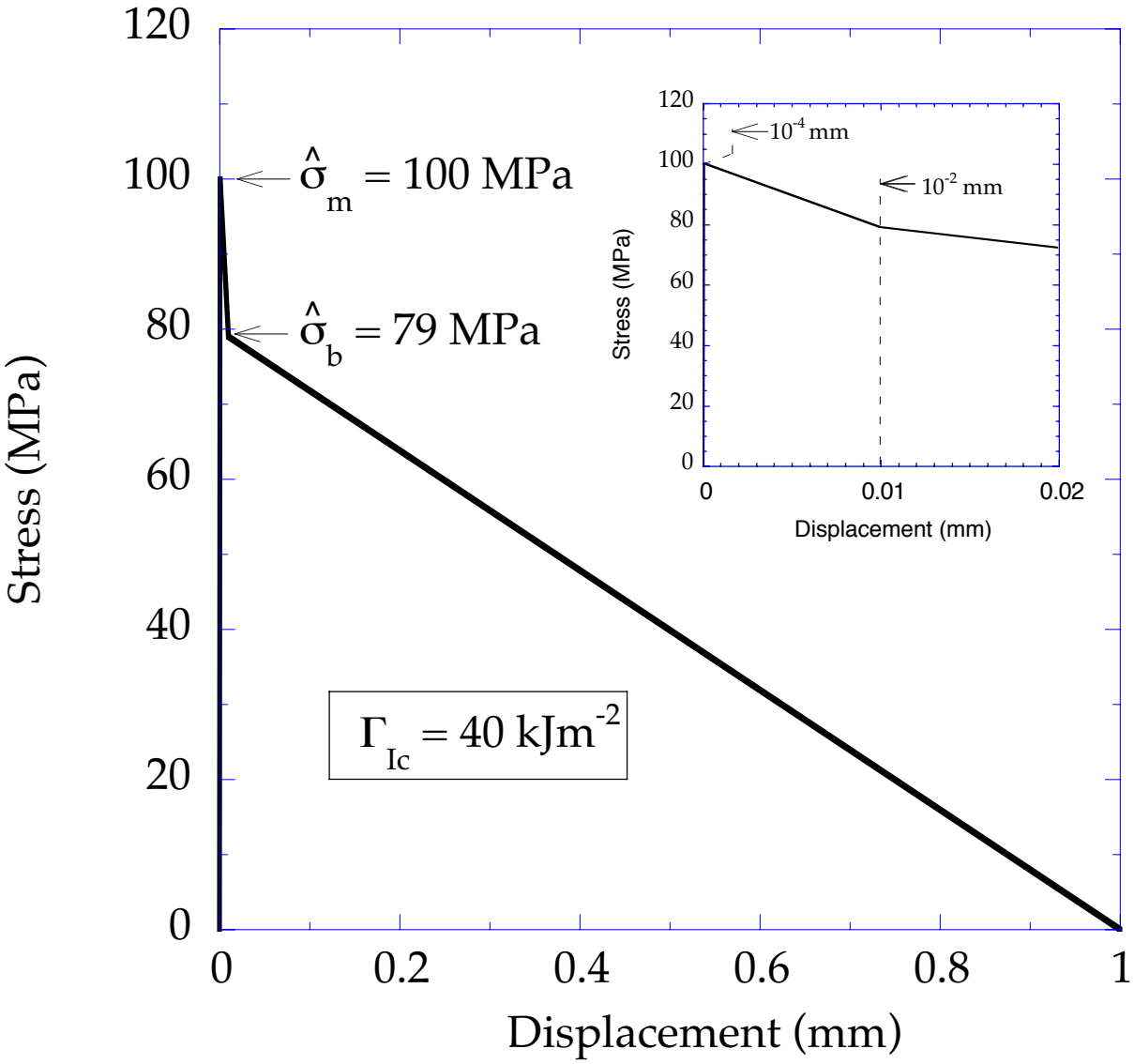
120
100
80
60
40
20
0
Stress (MPa)
$\hat{\sigma}_m = 100$ MPa
$\hat{\sigma}_b = 79$ MPa
$\Gamma_{Ic} = 40$ kJm^{-2}
0
0.2
0.4
0.6
0.8
1
Displacement (mm)
10^{-4} mm
10^{-2} mm
Stress (MPa)
0.01
0.02
Displacement (mm)

Figure 1

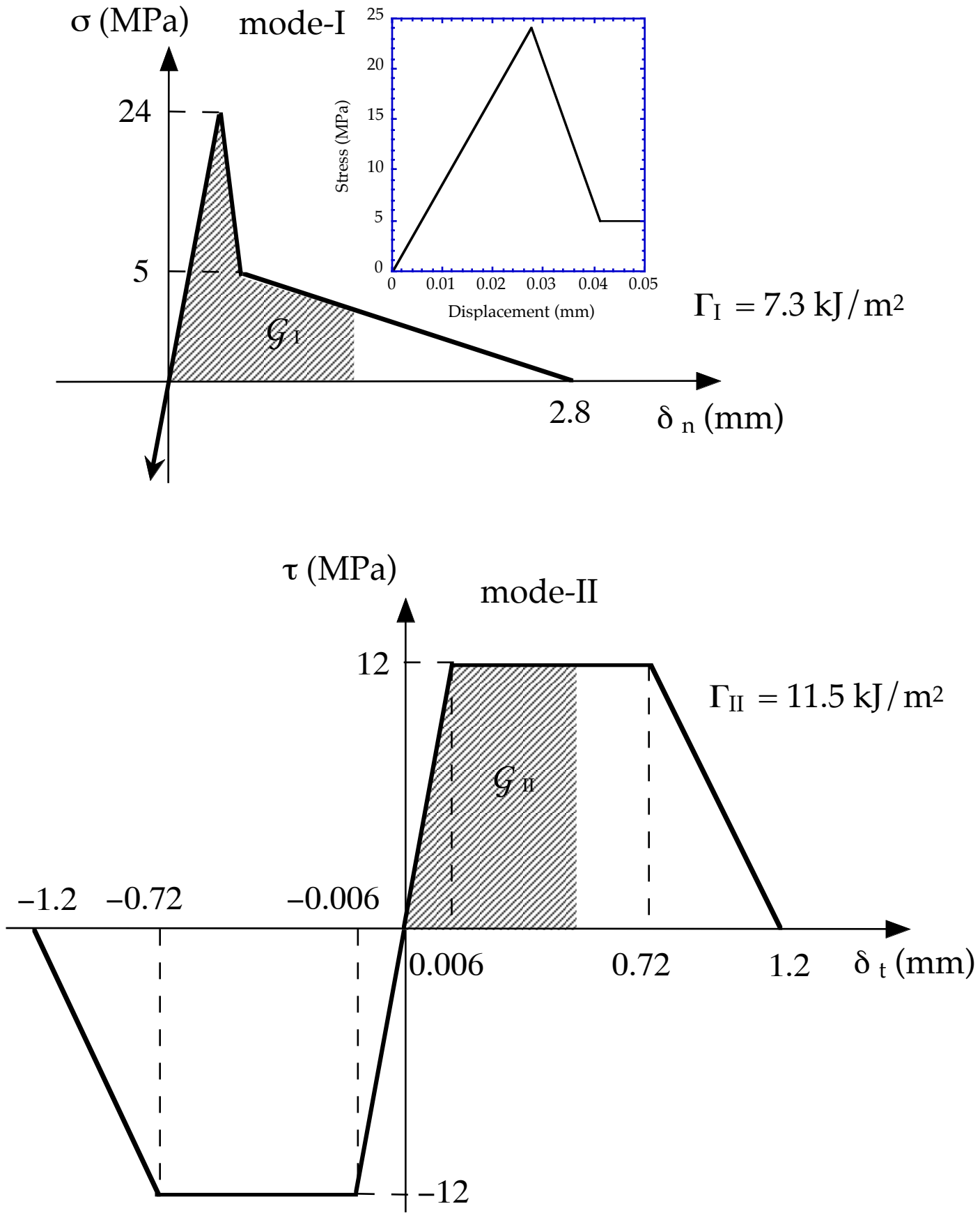
σ (MPa)
mode-I
24
5
2.8
δ n (mm)
Γ I = 7.3 kJ/m2
Stress (MPa)
Displacement (mm)
τ (MPa)
mode-II
12
−12
−1.2
−0.72
−0.006
0.006
0.72
1.2
δ t (mm)
Γ II = 11.5 kJ/m2

Figure 2

width (out of plane): 25 mm

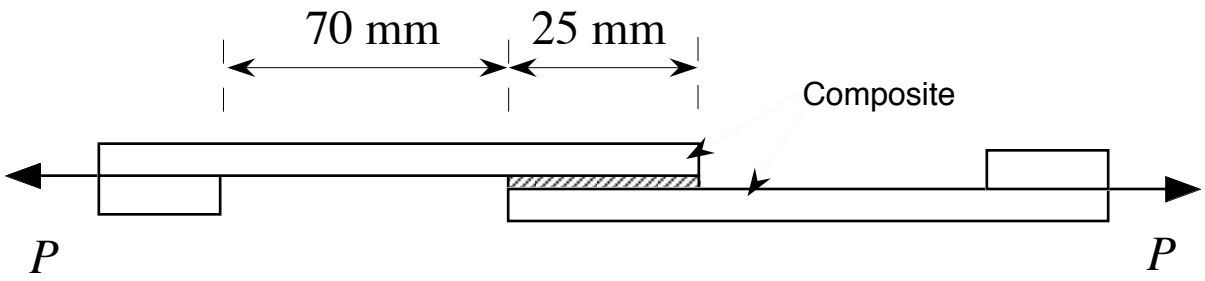

Figure 3a

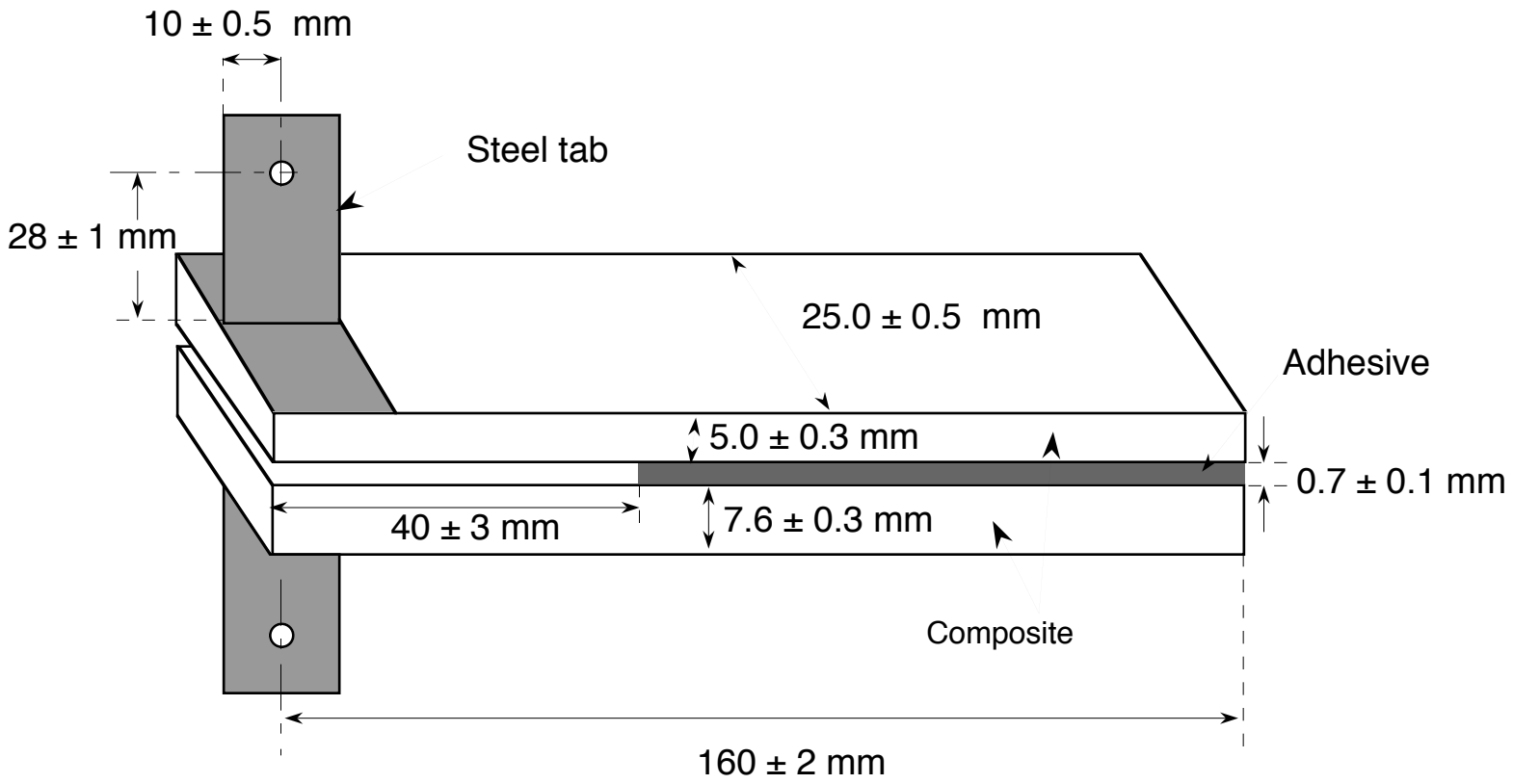
10 ± 0.5 mm
Steel tab
28 ± 1 mm
25.0 ± 0.5 mm
Adhesive
5.0 ± 0.3 mm
0.7 ± 0.1 mm
40 ± 3 mm
7.6 ± 0.3 mm
Composite
160 ± 2 mm

Figure 3b

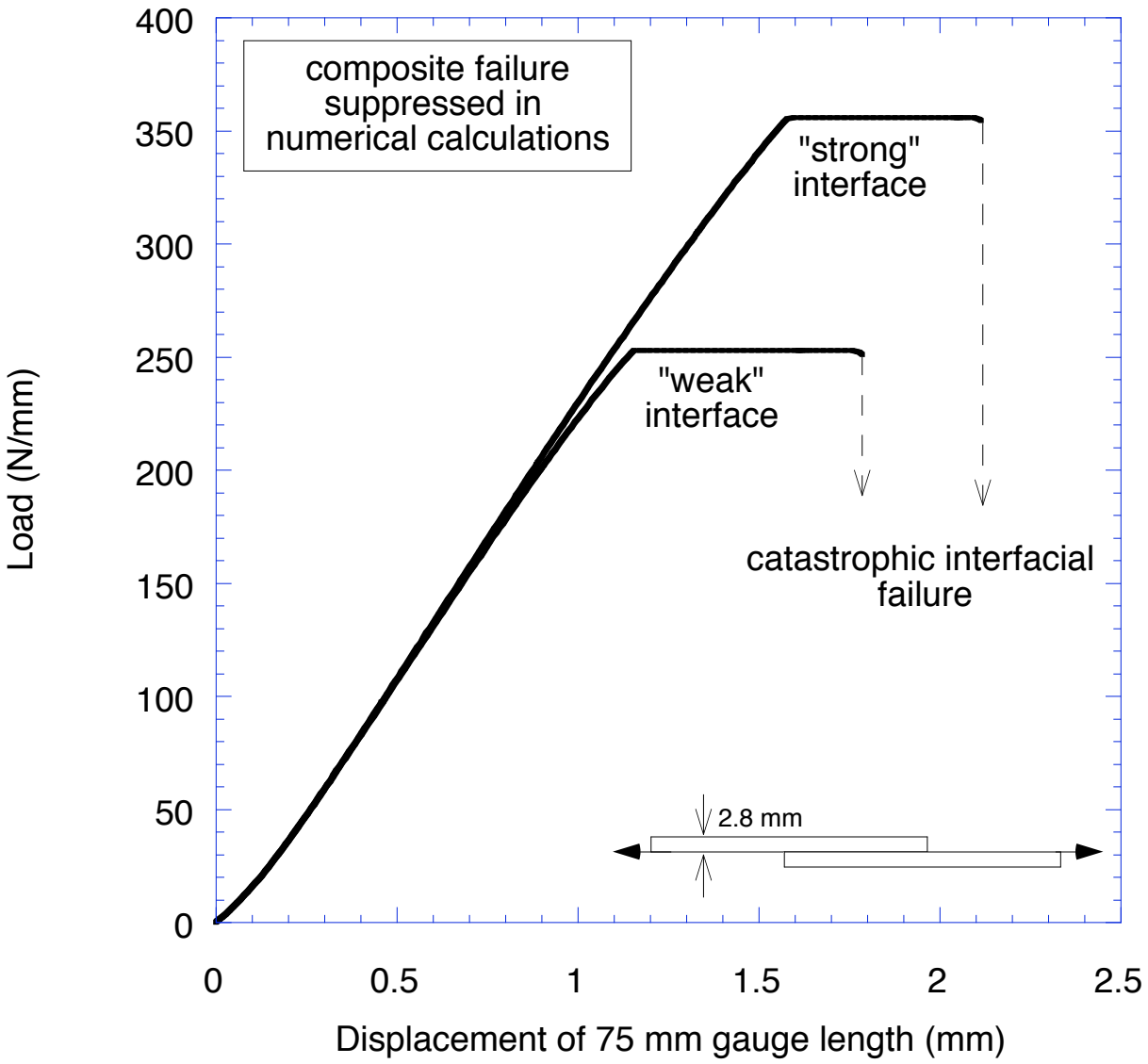
composite failure suppressed in numerical calculations
"strong" interface
"weak" interface
catastrophic interfacial failure
2.8 mm
Load (N/mm)
Displacement of 75 mm gauge length (mm)
400
350
300
250
200
150
100
50
0
0
0.5
1
1.5
2
2.5

Figure 4a

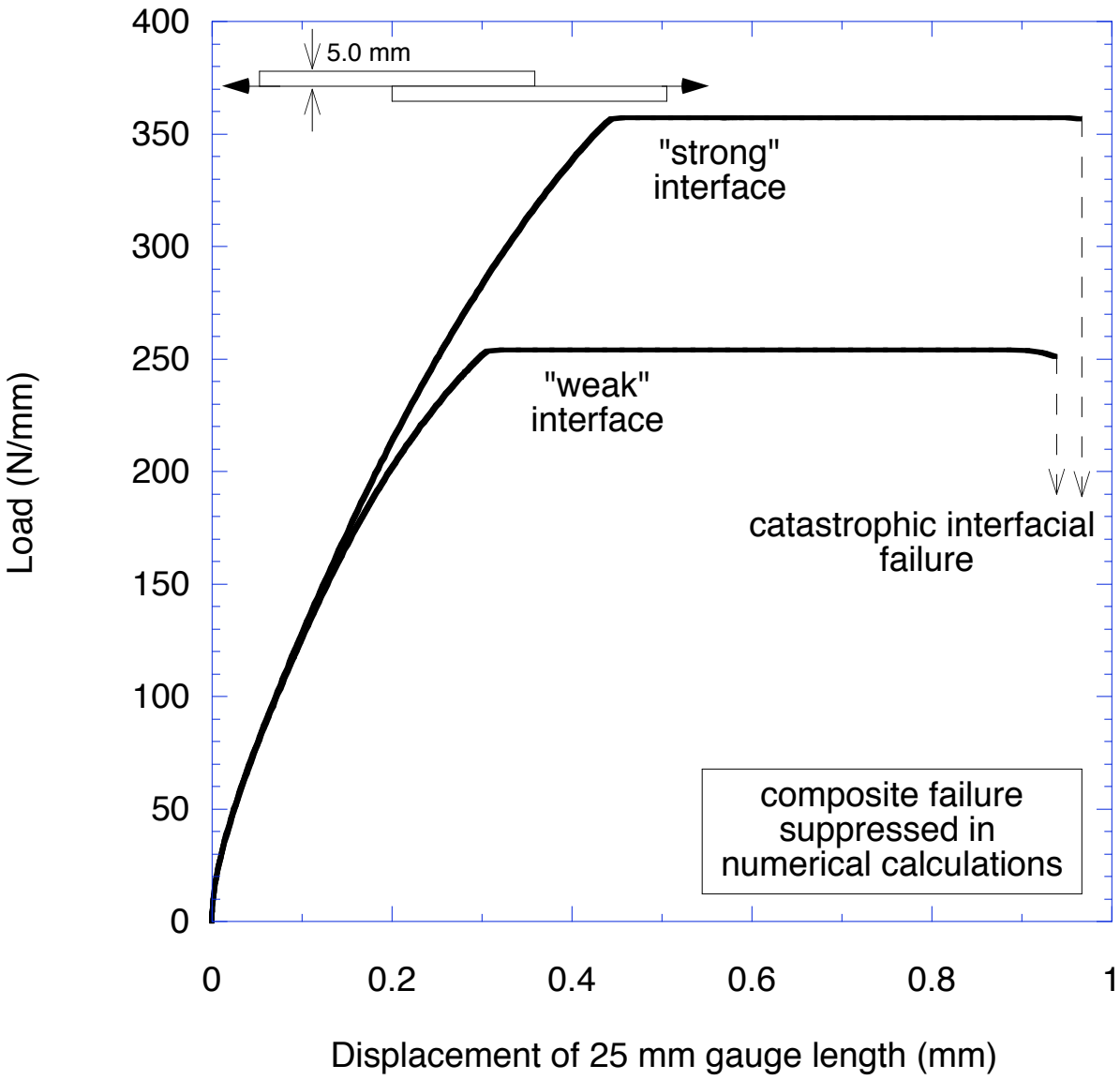
400
350
300
250
200
150
100
50
0
0
0.2
0.4
0.6
0.8
1
Load (N/mm)
Displacement of 25 mm gauge length (mm)
5.0 mm
"strong"
interface
"weak"
interface
catastrophic interfacial
failure
composite failure
suppressed in
numerical calculations

Figure 4b

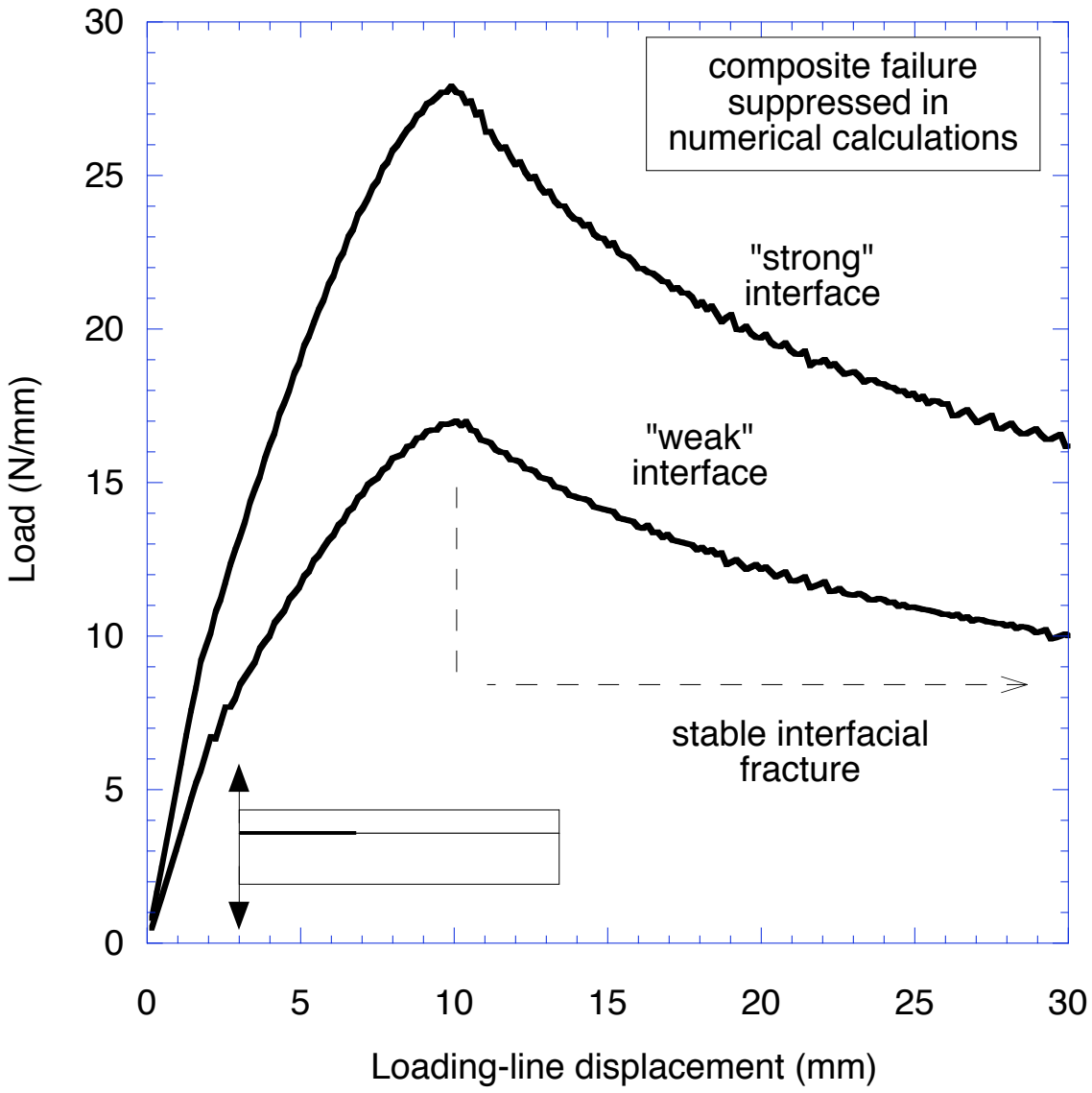
composite failure
suppressed in
numerical calculations
"strong"
interface
"weak"
interface
stable interfacial
fracture
Load (N/mm)
Loading-line displacement (mm)
0
5
10
15
20
25
30

Figure 4c

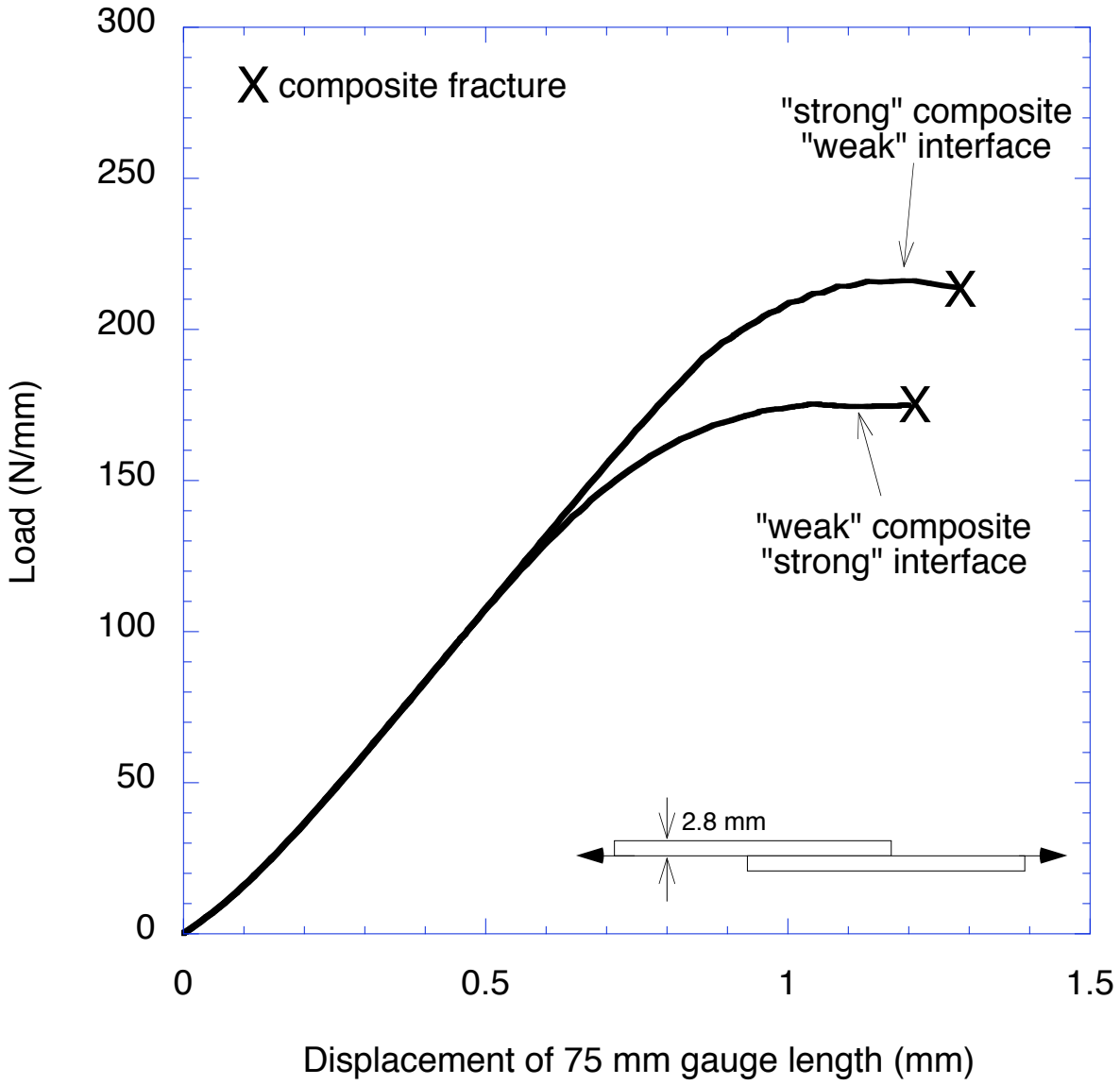
300
250
200
150
100
50
0
Load (N/mm)
X composite fracture
"strong" composite
"weak" interface
"weak" composite
"strong" interface
2.8 mm
0
0.5
1
1.5
Displacement of 75 mm gauge length (mm)

Figure 5a

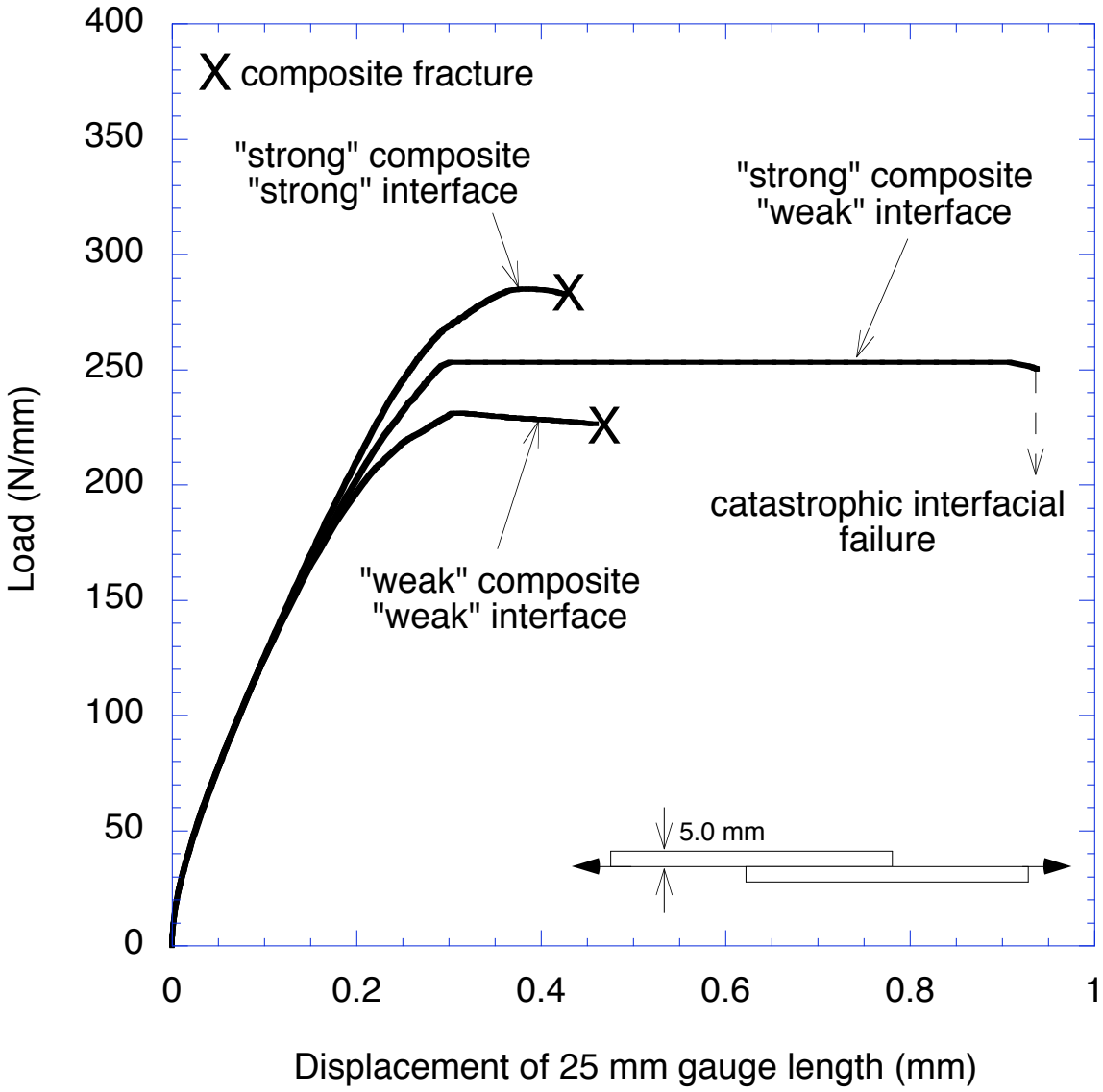
X composite fracture
"strong" composite
"strong" interface
"strong" composite
"weak" interface
catastrophic interfacial
failure
"weak" composite
"weak" interface
5.0 mm
Load (N/mm)
Displacement of 25 mm gauge length (mm)
400
350
300
250
200
150
100
50
0
0
0.2
0.4
0.6
0.8
1

Figure 5b

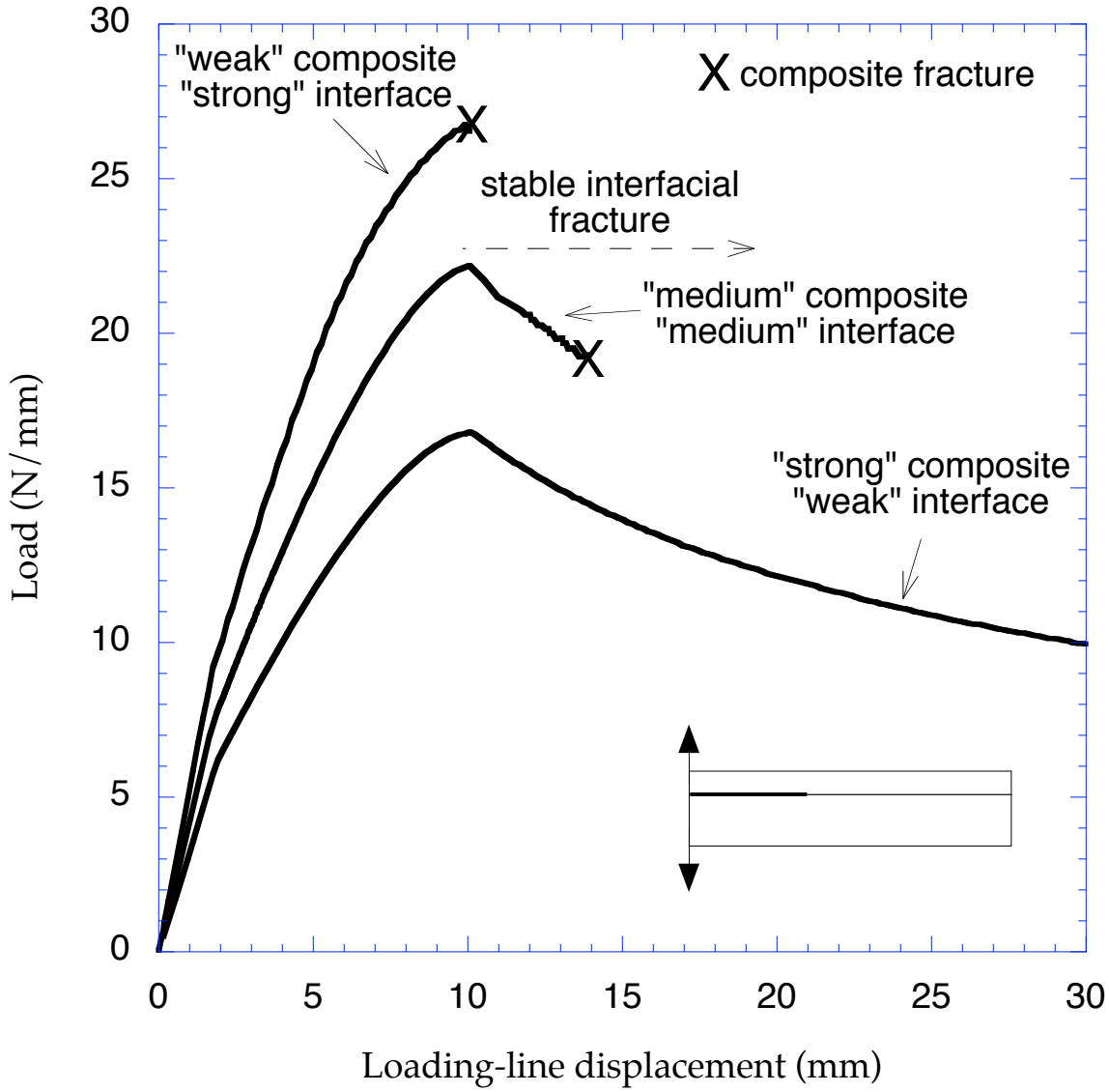
"weak" composite
"strong" interface
X composite fracture
stable interfacial
fracture
"medium" composite
"medium" interface
"strong" composite
"weak" interface
Load (N/mm)
Loading-line displacement (mm)
0
5
10
15
20
25
30

Figure 5c

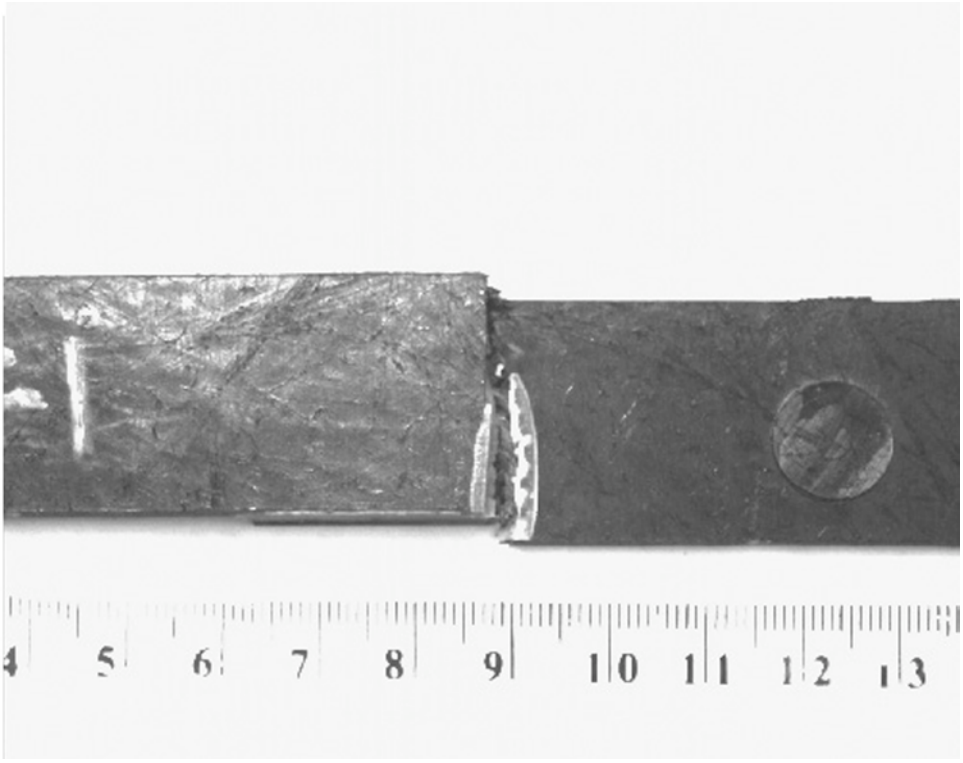

Figure 6a

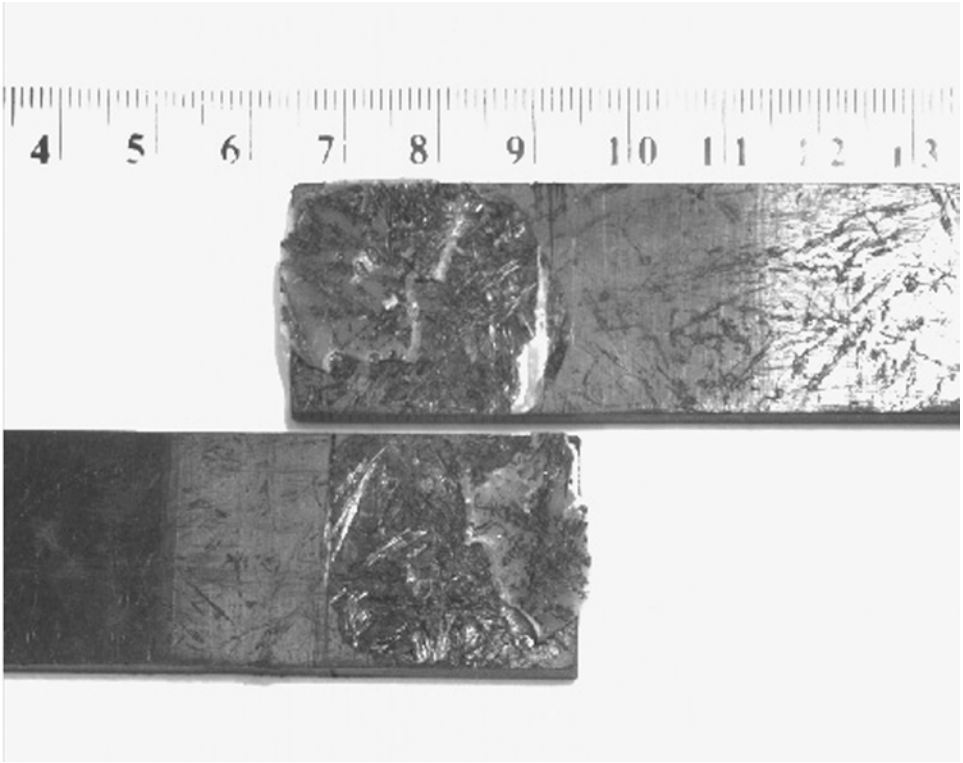

Figure 6b

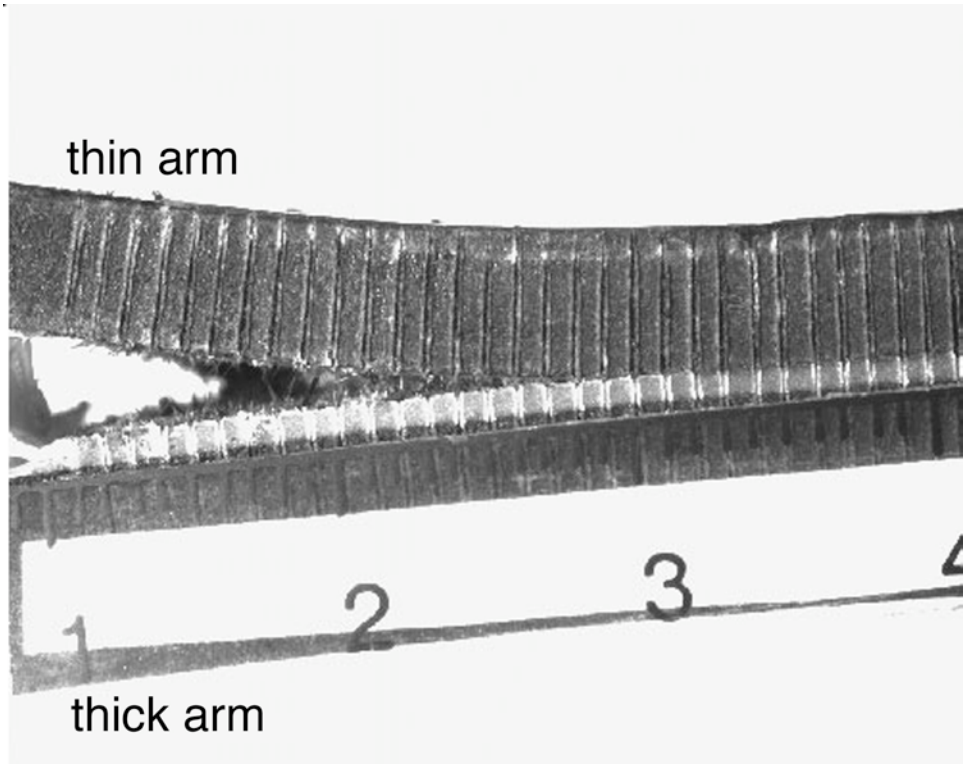

Figure 7a

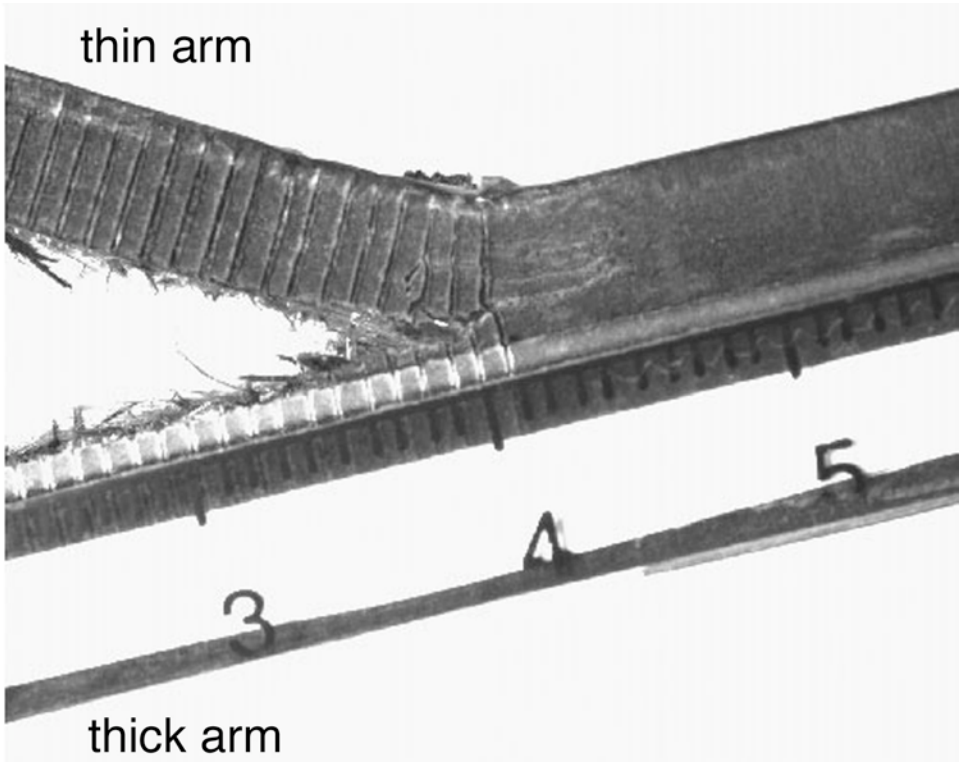

Figure 7b

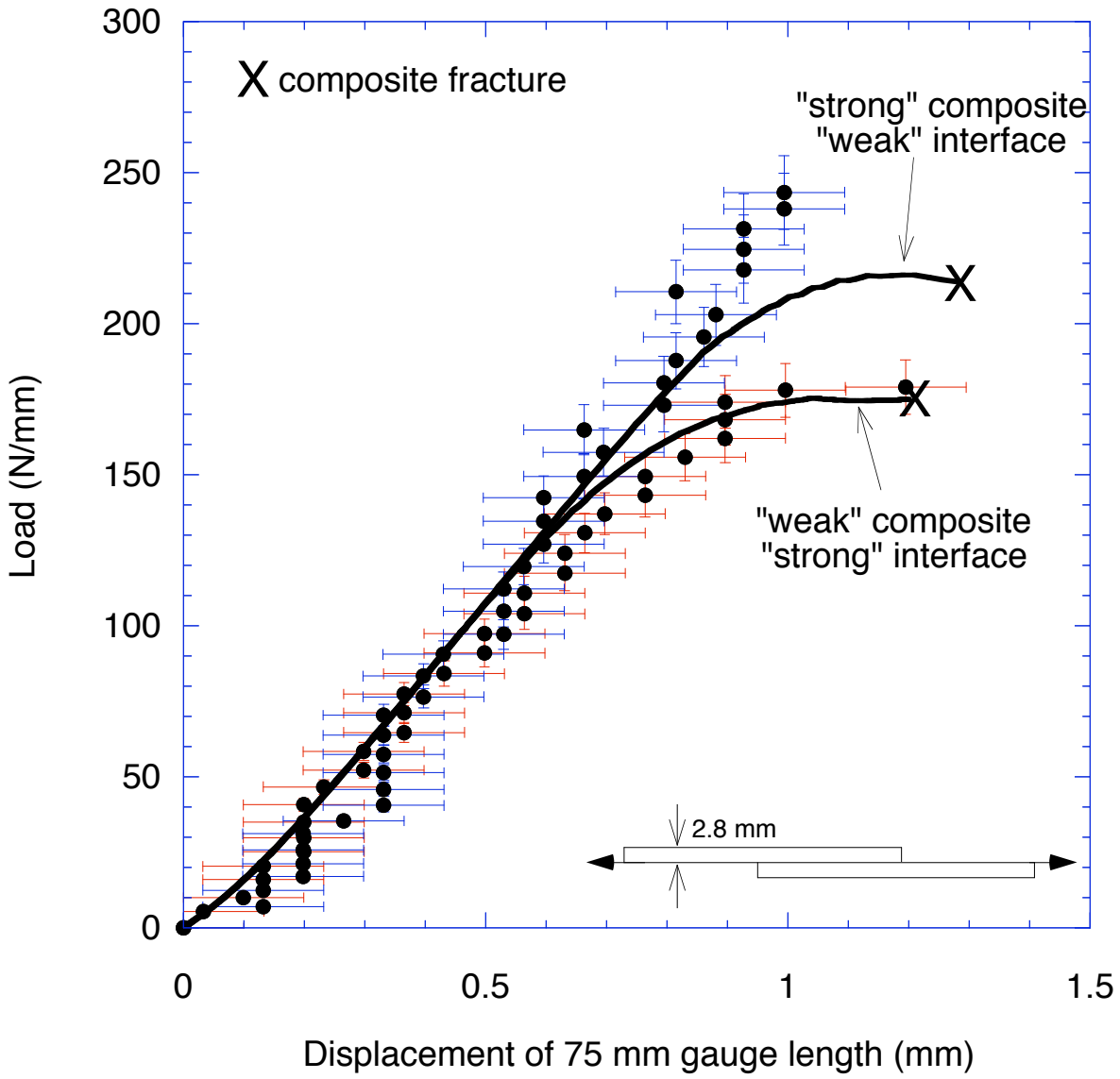
X composite fracture
"strong" composite
"weak" interface
"weak" composite
"strong" interface
2.8 mm
Load (N/mm)
Displacement of 75 mm gauge length (mm)
300
250
200
150
100
50
0
0
0.5
1
1.5

Figure 8a

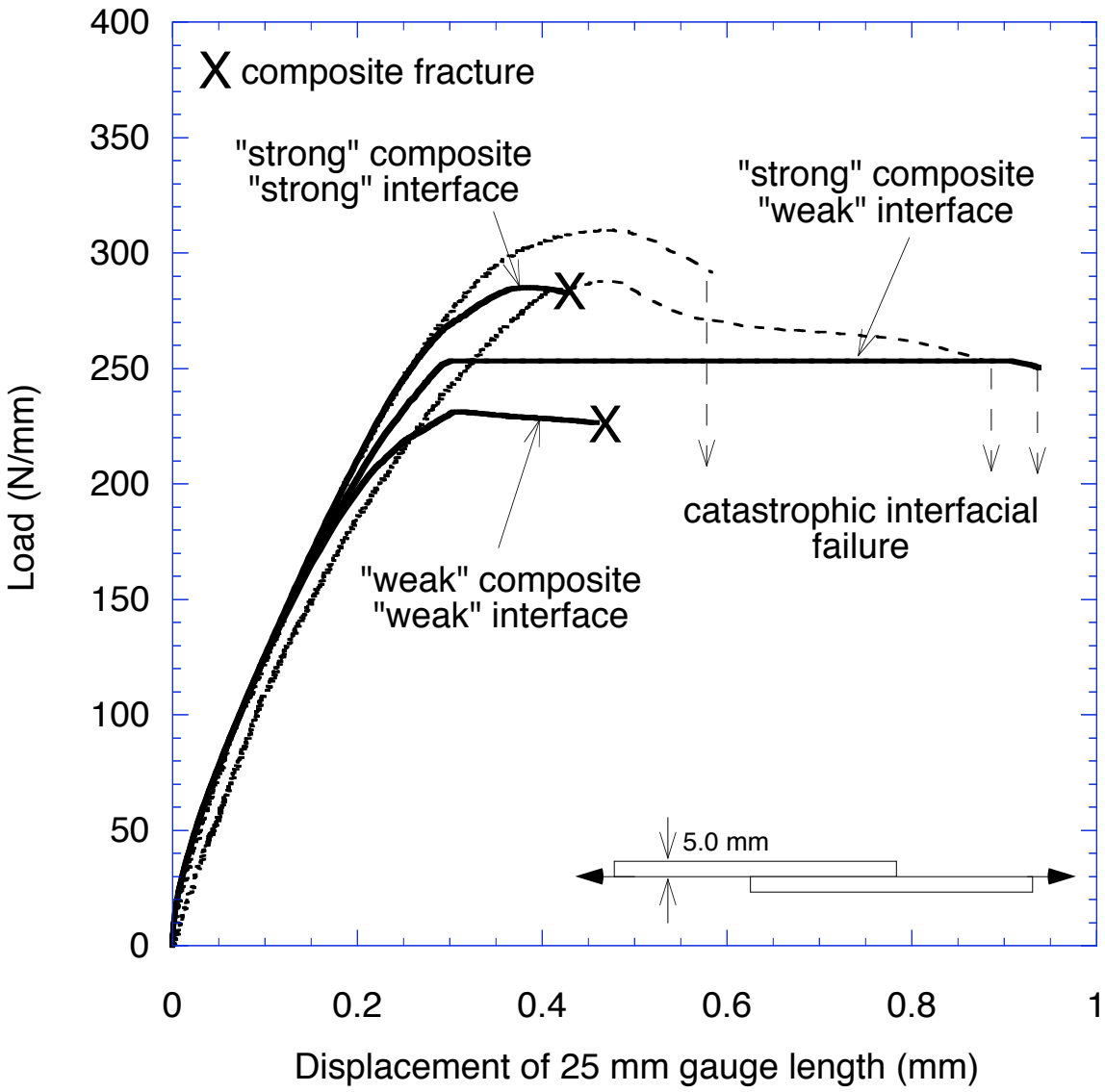
X composite fracture
"strong" composite
"strong" interface
"strong" composite
"weak" interface
catastrophic interfacial
failure
"weak" composite
"weak" interface
5.0 mm
Load (N/mm)
Displacement of 25 mm gauge length (mm)
0
50
100
150
200
250
300
350
400
0
0.2
0.4
0.6
0.8
1

Figure 8b

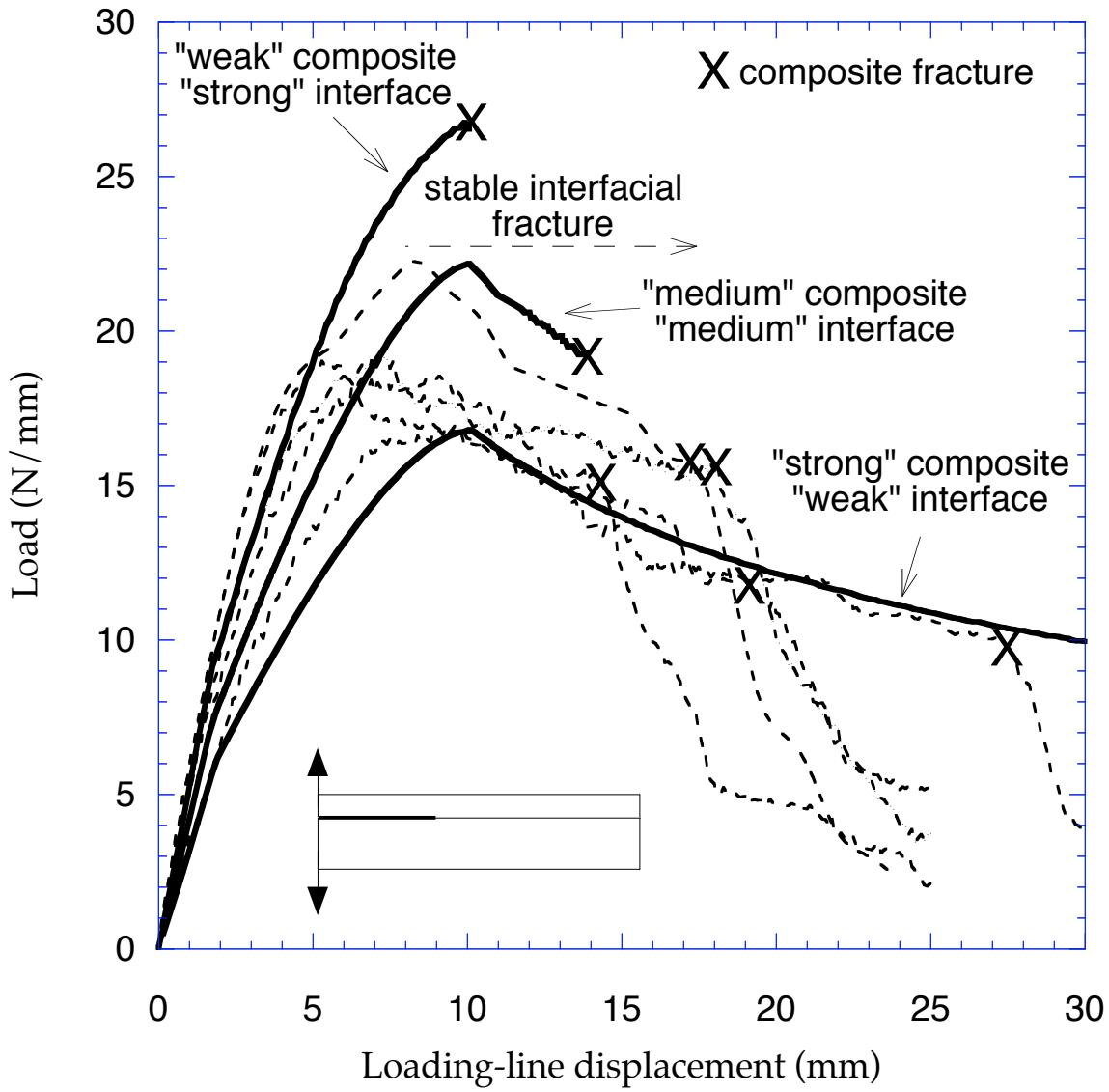
"weak" composite
"strong" interface
X composite fracture
stable interfacial
fracture
"medium" composite
"medium" interface
"strong" composite
"weak" interface
Load (N/mm)
Loading-line displacement (mm)
0
5
10
15
20
25
30

Figure 8c